

Bayesian inference of neutron-skin thickness and neutron-star observables based on effective nuclear interactions

Jia Zhou^{1,2} and Jun Xu^{3,1,*}

¹*Shanghai Institute of Applied Physics, Chinese Academy of Sciences, Shanghai 201800, China*

²*University of Chinese Academy of Sciences, Beijing 100049, China*

³*School of Physics Science and Engineering, Tongji University, Shanghai 200092, China*

We have obtained the constraints on the density dependence of the symmetry energy from neutron-skin thickness data by parity-violating electron scatterings and neutron-star observables using a Bayesian approach, based on the standard Skyrme-Hartree-Fock (SHF) model and its extension as well as the relativistic mean-field (RMF) model. While the neutron-skin thickness data (neutron-star observables) mostly constrain the symmetry energy at subsaturation (suprasaturation) densities, they may more or less constrain the behavior of the symmetry energy at suprasaturation (subsaturation) densities, depending on the energy-density functional form. Besides showing the final posterior density dependence of the symmetry energy, we also compare the slope parameters of the symmetry energy at 0.10 fm^{-3} as well as the values of the symmetry energy at twice saturation density from three effective nuclear interactions. The present work serves as a comparison study based on relativistic and nonrelativistic energy-density functionals for constraining the nuclear symmetry energy from low to high densities using a Bayesian approach.

I. INTRODUCTION

The nuclear symmetry energy $E_{sym}(\rho)$ is one of the most uncertain part of the nuclear matter equation of state (EOS), and great efforts have been devoted to extract its density dependence in the past twenty years [1–3]. While the nuclear symmetry energy may affect properties of various nuclear systems from finite nuclei to neutron stars [1, 2], different observables are sensitive to the $E_{sym}(\rho)$ at different density regions [4]. For example, the neutron-skin thickness of a nucleus is most sensitive to the slope parameter of the $E_{sym}(\rho)$ around $\rho = 2\rho_0/3$ [5, 6], with ρ_0 being the saturation density, while the radius of a neutron star is most sensitive to the $E_{sym}(\rho)$ around and above ρ_0 [2, 7, 8]. Combining the data of neutron-skin thickness and neutron stars may help to constrain the nuclear matter EOS, particularly the $E_{sym}(\rho)$, from low to high densities [9–13].

The recent PREX and CREX experiments have provided the data of the neutron-skin thickness for ^{208}Pb [14] and ^{48}Ca [15], with the former (latter) favoring a large (small) slope parameter L of the $E_{sym}(\rho)$. While the measurement through the parity-violating electron-nucleus scatterings is less model-dependent, the large error bars of the corresponding experimental data may limit the constraining power on the L , and it is of interest to see how $E_{sym}(\rho)$ is constrained from both PREX and CREX data. Besides the neutron-skin thickness from light to heavy nuclei, the emergence of recent neutron-star observables, especially the neutron-star radius, provides good opportunities to constrain the $E_{sym}(\rho)$ at suprasaturation densities. Recently, the GW170817 event [16] analyzed by the LIGO Scientific Collaboration and Virgo Collaboration as well as the

PSR J0030+0451 [17] and PSR J0740+6620 [18] measured by NICER have provided high-quality data for both neutron-star radii and masses, putting constraints on $E_{sym}(\rho)$ at high densities characterized by not only the slope parameter L but also higher-order EOS parameters (see, e.g., Refs. [19–21]).

To take good use of many data sets in various systems from finite nuclei to neutron stars including those mentioned above, the Bayesian analysis serves as a good tool to give quantitative constraints on model parameters. On the other hand, the results of such analysis generally depend on the particular theoretical model employed in the study, which uses model parameters as input and provides results of observables as output. In the present study, we employ non-relativistic and relativistic effective nuclear interactions, in order to check with the model dependence on the constraints of the $E_{sym}(\rho)$. For the non-relativistic effective nuclear interaction, we use the standard SHF model as well as its extension, i.e., the Korea-IBS-Daegu-SKKU (KIDS) model. For the relativistic effective nuclear interaction, we use the relativistic mean-field (RMF) model with σ , ω , and ρ mesons. The advantages of using these energy-density functionals (EDFs) is that one can express inversely model coefficients in terms of macroscopic physics quantities [22–24]. In that case, one can then set these macroscopic physics quantities as model parameters, so that the sampling in the parameter space becomes more efficient in the Bayesian analysis. The present study could be considered as one of the applications of the machine learning in nuclear physics (see, e.g., Refs. [25–31]).

The rest part of the paper is organized as follows. Section II provides briefly the theoretical framework, including an introduction of the standard SHF model as well as its extension and the RMF model, the calculation method of nucleon density distributions in finite nuclei and neutron-star properties, and the Bayesian analysis method. Section III provides constraints on the parame-

* Correspond to junxu@tongji.edu.cn

ters of the $E_{sym}(\rho)$ as well as its density dependence from different observables based on three effective nuclear interactions using the Bayesian approach. We conclude and outlook in Sec. IV.

II. THEORETICAL FRAMEWORK

In the standard SHF model, the effective interaction between two nucleons at the positions \vec{r}_1 and \vec{r}_2 is expressed as

$$\begin{aligned} v^{SHF}(\vec{r}_1, \vec{r}_2) = & t_0(1 + x_0 P_\sigma) \delta(\vec{r}) \\ & + \frac{1}{2} t_1(1 + x_1 P_\sigma) [\vec{k}'^2 \delta(\vec{r}) + \delta(\vec{r}) \vec{k}^2] \\ & + t_2(1 + x_2 P_\sigma) \vec{k}' \cdot \delta(\vec{r}) \vec{k} \\ & + \frac{1}{6} t_3(1 + x_3 P_\sigma) \rho^\alpha(\vec{R}) \delta(\vec{r}) \\ & + iW_0(\vec{\sigma}_1 + \vec{\sigma}_2) [\vec{k}' \times \delta(\vec{r}) \vec{k}]. \end{aligned} \quad (1)$$

In the above, $\vec{r} = \vec{r}_1 - \vec{r}_2$ is the relative coordinate of the two nucleons, $\vec{R} = (\vec{r}_1 + \vec{r}_2)/2$ is their central coordinate with $\rho(\vec{R})$ being the nucleon density there, $\vec{k} = (\nabla_1 - \nabla_2)/2i$ is the relative momentum operator and \vec{k}' is its complex conjugate acting on the left, and $P_\sigma = (1 + \vec{\sigma}_1 \cdot \vec{\sigma}_2)/2$ is the spin exchange operator, with $\vec{\sigma}_{1(2)}$ being the Pauli matrices acting on nucleon 1(2). While the coefficient of the spin-orbit interaction is fixed at $W_0 = 133$ MeV fm⁵, the other nine parameters in the Skyrme interaction $t_0, t_1, t_2, t_3, x_0, x_1, x_2, x_3$, and α can be expressed analytically in terms of nine macroscopic quantities, i.e., the saturation density ρ_0 , the binding energy E_0 , and the incompressibility K_0 of symmetric nuclear matter at ρ_0 , the isoscalar and isovector nucleon effective mass m_s^* and m_v^* in normal nuclear matter, the symmetry energy E_{sym}^0 and its slope parameter L at ρ_0 , and the isoscalar and isovector density gradient coefficient G_S and G_V . For more details, we refer the reader to Ref. [22].

As an extension of the above standard SHF EDF, the density-dependent term in the effective interaction [Eq. (1)] is replaced by the following term in the KIDS model

$$v_\rho^{KIDS}(\vec{r}_1, \vec{r}_2) = \frac{1}{6} \sum_{i=1}^3 (t_{3i} + y_{3i} P_\sigma) \rho^{i/3}(\vec{R}) \delta(\vec{r}). \quad (2)$$

Compared to the standard SHF model, there are three additional coefficients, which allows us to vary three more independent macroscopic quantities, i.e., the skewness EOS parameter Q_0 of symmetric nuclear matter, and the curvature parameter K_{sym} as well as the skewness parameter Q_{sym} of the symmetry energy at ρ_0 . For more details, we refer the reader to Ref. [23].

Based on the effective interaction, the EDF can then be obtained using the Hartree-Fock method, and the single-particle Hamiltonian is obtained using the variational principle, with the Coulomb interaction also explicitly included. Solving the Schrödinger equation gives

the wave functions of constituent neutrons and protons and thus their density distributions, and the neutron-skin thickness can then be obtained from the difference in the root-mean-square radii of neutrons and protons. For details of this standard procedure, we refer the reader to Ref. [32]. In the present work, we use Reinhard's code described in Ref. [33] for the standard SHF model, and with some modifications on the density-dependent term for the KIDS model.

For the RMF model, we take the following Lagrangian form

$$\mathcal{L} = \mathcal{L}_{nm} + \mathcal{L}_\sigma + \mathcal{L}_\omega + \mathcal{L}_\rho + \mathcal{L}_{\omega\rho}, \quad (3)$$

with

$$\begin{aligned} \mathcal{L}_{nm} = & \bar{\psi}(i\gamma^\mu \partial_\mu - m)\psi + g_\sigma \sigma \bar{\psi}\psi - g_\omega \bar{\psi}\gamma^\mu \omega_\mu \psi, \\ & - \frac{g_\rho}{2} \bar{\psi}\gamma^\mu \vec{\rho}_\mu \vec{\tau}\psi, \\ \mathcal{L}_\sigma = & \frac{1}{2} (\partial^\mu \sigma \partial_\mu \sigma - m_\sigma^2 \sigma^2) - \frac{A}{3} \sigma^3 - \frac{B}{4} \sigma^4, \\ \mathcal{L}_\omega = & -\frac{1}{4} F^{\mu\nu} F_{\mu\nu} + \frac{1}{2} m_\omega^2 \omega_\mu \omega^\mu + \frac{C}{4} (g_\omega^2 \omega_\mu \omega^\mu)^2, \\ \mathcal{L}_\rho = & -\frac{1}{4} \vec{B}^{\mu\nu} \vec{B}_{\mu\nu} + \frac{1}{2} m_\rho^2 \vec{\rho}_\mu \vec{\rho}^\mu, \\ \mathcal{L}_{\omega\rho} = & \frac{1}{2} \alpha'_3 g_\omega^2 g_\rho^2 \omega_\mu \omega^\mu \vec{\rho}_\mu \vec{\rho}^\mu. \end{aligned}$$

In the above, \mathcal{L}_{nm} represents the contribution from the kinetic part of nucleons as well as its coupling to σ , ω , and ρ mesons, with ψ , σ , ω_μ , and $\vec{\rho}_\mu$ being the fields of nucleons and corresponding mesons, where g_ρ , g_ω , and g_ρ are the corresponding coupling constants, and $\vec{\tau}$ is the Pauli matrices in isospin space. \mathcal{L}_σ , \mathcal{L}_ω , and \mathcal{L}_ρ contain free and self-interacting terms of σ , ω , and ρ mesons, respectively, and $\mathcal{L}_{\omega\rho}$ represents the cross interaction term between ω and ρ mesons. The antisymmetric field tensors $F_{\mu\nu}$ and $\vec{B}_{\mu\nu}$ are defined as $F_{\mu\nu} = \partial_\nu \omega_\mu - \partial_\mu \omega_\nu$ and $\vec{B}_{\mu\nu} = \partial_\nu \vec{\rho}_\mu - \partial_\mu \vec{\rho}_\nu - g_\rho (\vec{\rho}_\mu \times \vec{\rho}_\nu)$. For a given C , the six independent parameters g_σ^2/m_σ^2 , g_ω^2/m_ω^2 , g_ρ^2/m_ρ^2 , A , B , and α'_3 in the RMF model can be expressed inversely in terms of ρ_0 , E_0 , K_0 , E_{sym}^0 , L , and m_s^* as shown in Ref. [24]. The value of C can then be used to vary independently another macroscopic quantity, and we choose it as Q_0 as in Ref. [34].

Based on the mean-field approximation, the above fields are treated as classical ones. The Euler-Lagrange equations lead to the Dirac equations for nucleons and the Klein-Gordon equations for mesons, and they are solved in a coupled way to get the distributions of various fields in a nucleus, leading to the neutron and proton density distributions as well as the neutron-skin thickness. The calculation is based on the open source code in Ref. [35] after incorporating the non-linear self-interacting term for ω meson and the coupling between ρ and ω mesons.

The neutron-star part is calculated in the following way. We assume that the neutron star from the center

TABLE I. Prior ranges of model parameters in the standard SHF, KIDS, and RMF models for the Bayesian analysis in the present study.

	SHF	KIDS	RMF
K_0 (MeV)	220 – 260	220 – 260	220 – 260
Q_0 (MeV)	-	-800 – 400	-800 – 400
E_{sym}^0 (MeV)	28.5 – 34.9	28.5 – 34.9	28.5 – 34.9
L (MeV)	30 – 90	30 – 90	30 – 90
K_{sym} (MeV)	-	-400 – 100	-
Q_{sym} (MeV)	-	-200 – 800	-
m_s^*/m	0.5 – 0.9	0.5 – 0.9	0.5 – 0.9
m_v^*/m	0.5 – 0.9	0.5 – 0.9	-

to the surface contains the liquid core of uniform neutron star matter, the inner crust consists of nuclear pasta phase, and the outer crust is composed of ion lattice and relativistic electron gas. The neutron star matter is formed by neutrons, protons, electrons, and possibly muons in the β -equilibrium and charge-neutrality condition, and the EOS is obtained from the EDFs of the standard SHF, KIDS, and RMF models described above. The transition density between the liquid core and the inner crust is self-consistently determined with a thermodynamical approach as detailed in Refs. [36, 37]. The EOS of the inner crust is parameterized based on an empirical polytropic relation between the pressure and the energy density [38–40]. For the EOS of the outer crust, we take the BPS EOS and the FMT EOS [41, 42]. Here we note that the crust EOS as well as the core-crust transition density may affect the constraints on the EOS from neutron-star observables (see, e.g., Ref. [34]). With the EOS at all density regions constructed above, the mass-radius relation of neutron stars can be calculated through the Tolman-Oppenheimer-Volkoff (TOV) equations.

The Bayesian analysis extracts posterior probability distribution functions (PDFs) of model parameters $M(p_1, p_2, p_3, \dots)$ by comparing results $D(d_1, d_2, d_3, \dots)$ from theoretical calculations to the experimental data. The numbers of model parameters, which are set as independent macroscopic quantities as described above, are different in the standard SHF, KIDS, and RMF models. In order to carry out a fair comparison for the three models, we have fixed $\rho_0 = 0.16 \text{ fm}^{-3}$ and $E_0 = -16 \text{ MeV}$ for all models, and $G_S = 132 \text{ MeV fm}^5$ and $G_V = 5 \text{ MeV fm}^5$ for the standard SHF and KIDS models, according to the empirical values of model parameters in Ref. [22]. We choose to vary $p_1 = K_0$ uniformly within 220 – 260 MeV from studies on isoscalar giant monopole resonances [43–47], and $p_2 = E_{sym}^0$ and $p_3 = L$ uniformly within 28.5 – 34.9 MeV and 30 – 90 MeV, respectively, according to Refs. [48, 49]. Higher-order EOS parameters $p_4 = K_{sym}$, $p_5 = Q_0$, and $p_6 = Q_{sym}$, if they can be changed as independent model parameters, are varied uniformly within their prior ranges obtained based on analyses of terrestrial nuclear experiments and EDFs [50, 51]. We also vary the non-relativistic isoscalar and isovector p-masses, i.e., $p_7 = m_s^*$ and $p_8 = m_v^*/m$, for

the standard SHF and KIDS model, and the isoscalar Dirac effective mass $p_7 = m_s^*/m$ for the RMF model. The prior ranges of model parameters are listed in Table I for different models, and in the Bayesian analysis a random walk is performed in such parameter space. As shown in Ref. [34], the real parameter space is smaller for the RMF model when we try to study properties of neutron stars, since there could be no solutions for the field equations at high densities. In the finite nuclei study, however, we have a larger parameter space for the RMF model compared to that in Ref. [34].

For neutron skins, how well the results d_i^{th} obtained from the theoretical model with model parameters p_i reproduce the experimental data d_i^{exp} is described by the likelihood function

$$P_{\Delta r_{np}} = \prod_{i=1,2} \left\{ \frac{1}{2\pi\sigma_i} \exp \left[-\frac{(d_i^{th} - d_i^{exp})^2}{2\sigma_i^2} \right] \right. \\ \times \left. \Theta \left(0.03 - \left| \frac{E_i^{th} - E_i^{exp}}{E_i^{exp}} \right| \right) \Theta \left(0.03 - \left| \frac{r_i^{th} - r_i^{exp}}{r_i^{exp}} \right| \right) \right\} \quad (4)$$

Here $i = 1$ and 2 represent data of ^{208}Pb and ^{48}Ca , respectively. We choose the neutron-skin thickness data $\Delta r_{np} = 0.283 \pm 0.071 \text{ fm}$ for ^{208}Pb from PREX [14] and $\Delta r_{np} = 0.121 \pm 0.035 \text{ fm}$ for ^{48}Ca from CREX [15], so $d_{1,2}$ and $\sigma_{1,2}$ in Eq. (4) are chosen to be the mean value and 1σ error, respectively. While each theoretical model can reproduce the experimental data of the binding energy E_i^{exp} and the charge radius r_i^{exp} taken from Refs. [52, 53] in a higher accuracy, here we allow a rather extensive error 3% so that the extracted constraints on the EOS are from neutron-skin data rather than from E_i^{exp} and r_i^{exp} .

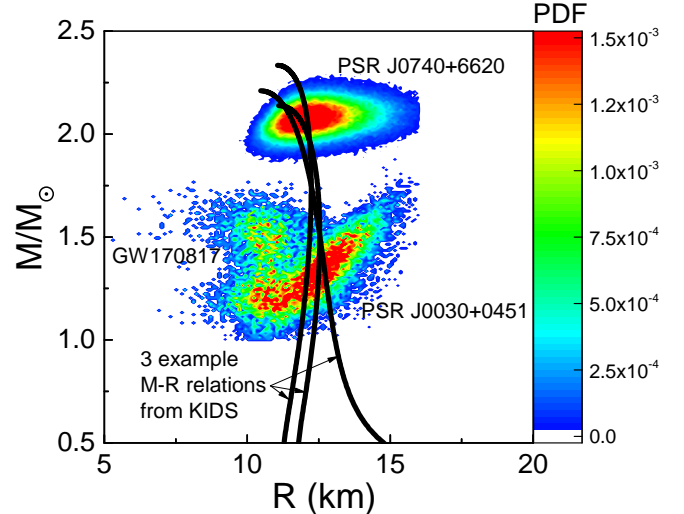


FIG. 1. Two-dimensional PDFs from the sampling data of the GW170817 event as well as the PSR J0030+0451 and the PSR J0740+6620 in the mass-radius ($M - R$) plane. Three highly favored representative $M - R$ relations from the KIDS model, which pass through the most probable regions of the PDFs, are plotted for illustration.

From the GW170817 event measured by the LIGO Scientific Collaboration and Virgo Collaboration, the radii of the binary stars were measured to be $R_1 = 10.8^{+2.0}_{-1.7}$ km and $R_2 = 10.7^{+2.1}_{-1.5}$ km from the EOS-insensitive-relation analysis, with the masses M_1 within $[1.36, 1.62]M_\odot$ and M_2 within $[1.15, 1.36]M_\odot$, where M_\odot is the solar mass, and a tidal deformability $\Lambda_{1.4} = 190^{+390}_{-120}$ for canonical neutron stars is also inferred from the GW170817 data at the 90% confidence level [16]. More recently, the mass and the radius of the pulsar PSR J0030+0451 were obtained to be $1.34^{+0.15}_{-0.16}M_\odot$ and $12.71^{+1.14}_{-1.19}$ km [17], respectively, and those of the pulsar PSR J0740+6620 were constrained to be $2.072^{+0.067}_{-0.066}M_\odot$ and $12.39^{+1.30}_{-0.98}$ km [18], respectively, at the 68% confidence level by NICER. In the present study, we construct the two-dimensional PDFs in the $M - R$ plane from the sampling data of the GW170817 event as well as the PSR J0030+0451 and the PSR J0740+6620, as that in Fig. 3 of Ref. [16], Fig. 20 of Ref. [17], and Fig. 7 of Ref. [18], respectively. The resulting PDFs for the three events are shown in Fig. 1, where three highly favored representative $M - R$ relations from the KIDS model, which pass through the most probable regions of the PDFs, are plotted for illustration. To be quantitative, we have mapped the two-dimensional PDFs $f_n(M, R)$ in the $M - R$ plane to $N_M \times N_R$ lattices, with $n = 1, 2$, and 3 representing the three astrophysical events, i.e., GW170817, PSR J0030+0451, and PSR J0740+6620, and $f_n(M, R)$ is normalized for each n . The likelihood function describing how well the resulting $M - R$ curve $M(R)$ reproduces the data is calculated by summing the values of $f_n(M, R)$ in the lattices along the trajectory of $M(R)$ and multiplying those for the three events, i.e.,

$$P_{MR} = \prod_{n=1}^3 \left[\sum_{j \in M(R)} f_n(M_j, R_j) \right]. \quad (5)$$

We use $N_M = 200$ and $N_R = 150$ in the present analysis, and their values may affect the resolution but may not affect the final results by much. In the summation of Eq. (5), we have also subtracted part of the $M(R)$ curve which represents an unstable neutron star or contains neutron-star matter that violates the causality condition, and the modified trajectory is expressed as $\tilde{M}(R)$.

The total likelihood function is $P = P_{\Delta r_{np}} \times P_{MR}$. According to the Bayes' theorem, the posterior PDF is the product of the likelihood function and the prior PDF with normalization. In the real calculation, the resulting posterior PDFs of EOS parameters from neutron-skin data or neutron-star data alone can be taken as the prior PDFs used for the second-round calculation, to achieve the final posterior PDFs from both neutron-skin and neutron-star data. For the algorithm of the Bayesian analysis, a Markov-Chain Monte Carlo approach using the Metropolis-Hastings algorithm is employed to reach an equilibrium distribution, with the relaxation process subtracted in the final analysis.

III. RESULTS AND DISCUSSIONS

We start by comparing the posterior PDFs of different symmetry energy parameters from the constraints of the neutron-skin thickness Δr_{np} data for ^{48}Ca and ^{208}Pb based on different effective nuclear interactions in Fig. 2. While E_{sym}^0 and L are anti-correlated from the constraint of Δr_{np} [6] based on the standard SHF model, the detailed behaviors of their posterior PDFs depend on their prior ranges (see, e.g., Fig. 4 in Ref. [23]), and a small (large) experimental value of Δr_{np} for ^{48}Ca (^{208}Pb) favors both small (large) E_{sym}^0 and L . In the standard SHF model where K_{sym} can't be varied independently, the Δr_{np} can't constrain K_{sym} . In the KIDS model where K_{sym} can be varied as an independent model parameter, the constraint on E_{sym}^0 becomes weaker while an opposite constraint on K_{sym} compared to that on L is observed. The latter is understandable since parameters of the symmetry energy at different orders compensate for each other. In the RMF model, some abnormal behaviors are observed, especially for the posterior PDFs of L and K_{sym} , and the explanations can be found in Appendix A. If we adopt both constraints of Δr_{np} for ^{48}Ca and ^{208}Pb , the resulting posterior PDFs are roughly the average of the PDFs from only ^{48}Ca or ^{208}Pb , which actually favor opposite trends of $E_{sym}(\rho)$ and corresponding parameters.

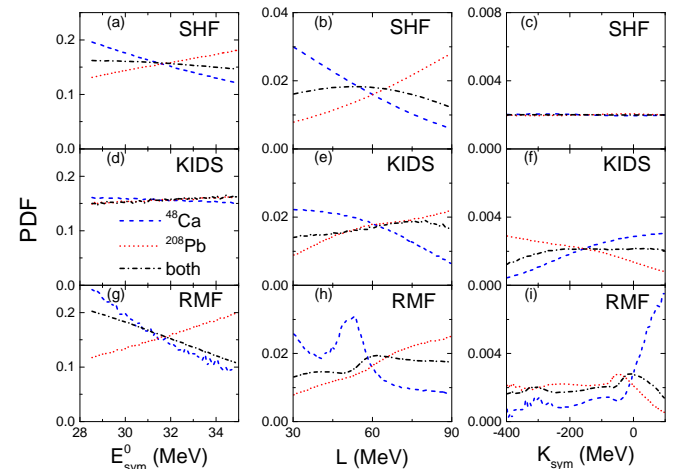


FIG. 2. Posterior PDFs of E_{sym}^0 (left), L (middle), and K_{sym} (right) from the neutron-skin thickness data of ^{48}Ca , ^{208}Pb , and both, based on the standard SHF, KIDS, and RMF models.

The posterior PDFs from both constraints of Δr_{np} for ^{48}Ca and ^{208}Pb are compared with those from neutron-star observables [34] in Fig. 3. It is seen that neutron-star observables generally favor a relatively smaller L but a larger K_{sym} , from respectively the constraints of the radii for neutron stars of intermediate to high masses from the three astrophysical events, compared to the constraints from the Δr_{np} for both ^{48}Ca and ^{208}Pb . It is noteworthy that the constraints on K_{sym} mostly come from neutron-

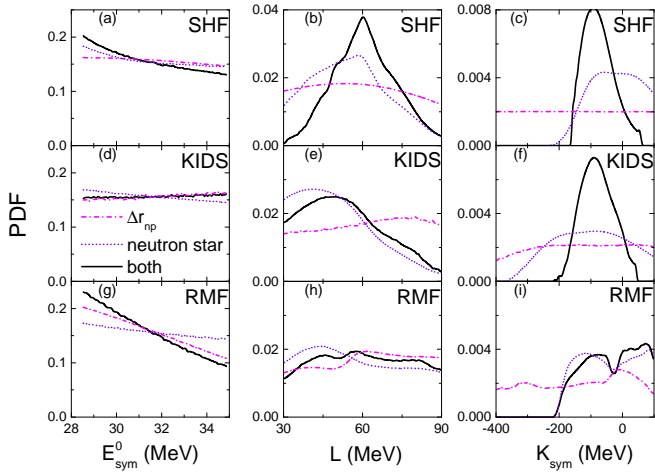


FIG. 3. Posterior PDFs of E_{sym}^0 (left), L (middle), and K_{sym} (right) from the neutron-skin thickness data, the neutron-star observables, and both data sets, based on the standard SHF, KIDS, and RMF models.

star observables rather than from Δr_{np} . The constraining powers on the symmetry energy parameters generally become enhanced after considering the data of neutron-star observables, especially for the standard SHF and KIDS models. The dip of the PDF of K_{sym} in the RMF model is from the parameter space with smaller m_s^* and larger L , which can not access a two-solar-mass neutron star, while other combinations of m_s^* and L which lead to the rest range of K_{sym} can explain better the astrophysical data. With the posterior PDFs shown in Figs. 2 and 3, we do see model dependence on the constraints of the E_{sym} parameters based on the same data set, depending on the EDF and the number of independent model parameters.

We compare the density dependence of the symmetry energy with prior distributions of model parameters and that from the constraints of Δr_{np} data, neutron-star observables, and both constraints in the density range from 0 to $3\rho_0$ in Fig. 4. The prior ranges of the symmetry energy are similar for the standard SHF and KIDS model, by adopting the prior ranges of independent model parameters as listed in Table I, except that KIDS allows an even softer symmetry energy. For the RMF model, as mentioned above, the larger parameter space for the study of finite nuclei leads to a larger prior range of $E_{sym}(\rho)$ compared to the neutron-star study in Ref. [34]. The Δr_{np} data put some constraints on the symmetry energy at subsaturation densities for all three models, especially for the RMF model by ruling out too large and unphysical $E_{sym}(\rho)$ at low densities, while the constraining power at high densities is weak. The neutron-star observables constrain appreciably the symmetry energy at suprasaturation densities, while the constraining power at subsaturation densities depends on the corresponding EDF form. The favored stiff E_{sym} in the RMF model from the constraint of neutron-star

observables is consistent with the behavior of the K_{sym} PDF shown in Fig. 3(i). Combining both constraints from Δr_{np} and neutron-star observables, the symmetry energies from low to high densities are nicely constrained. The constraining power is stronger for the standard SHF model and the RMF model, and weaker for the KIDS model, due to a larger number of independent model parameters in the KIDS model.

It is seen from Fig. 4 that incorporating the additional constraint of neutron-star observables (Δr_{np}) may further constrain the symmetry energy at low (high) densities, compared to the constraints of Δr_{np} (neutron-star observables) alone, according to the adopted energy-density functional. Here we illustrate the two situations separately. It has been shown that the Δr_{np} data generally constrains the slope parameter $L(\rho^*) = 3\rho^*(dE_{sym}/d\rho)_{\rho=\rho^*}$ of the symmetry energy at $\rho^* = 0.10$ fm $^{-3}$ [6, 54], and the posterior PDFs of $L(0.10)$ based on three different models are compared in the upper panel of Fig. 5. Model dependence is already observed here with only neutron-skin thickness data. If the constraint from neutron-star observables is further incorporated, the constraint on $L(0.10)$ is modified as shown in the lower panel of Fig. 5, and the difference among the three models becomes even larger. For the standard SHF model, the PDF of $L(0.10)$ becomes sharper after incorporating the constraints from neutron-star observables. For the KIDS model, the peak of the PDF of $L(0.10)$ moves to a lower side, and this is consistent with the behavior of $L(0.16)$ shown in Fig. 3(e). Actually, after including K_{sym} as an independent EOS variable, the strong correlation between Δr_{np} and $L(0.10)$ may not be rigorously valid (see, e.g., Ref. [23]). The behavior of the symmetry energy at suprasaturation densities is generally characterized by its value $E_{sym}(2\rho_0)$ at twice saturation density, with the fiducial value of about 47 MeV from various constraints as summarized in Ref. [55]. The posterior PDFs of $E_{sym}(2\rho_0)$ from neutron-star observables for the three models are compared in the upper panel of Fig. 6. The too large values of $E_{sym}(2\rho_0)$ for the standard SHF model, which is also observed in Fig. 4, is likely due to the constraint of the radii for large-mass neutron stars as well as the correlation between L and K_{sym} , and they are ruled out after further incorporating the constraint from Δr_{np} . On the other hand, the PDFs of $E_{sym}(2\rho_0)$ for the KIDS and RMF models are not much affected by further incorporating the constraint from Δr_{np} . This is again due to the less-flexible feature of the standard SHF model compared to the KIDS and RMF models.

IV. SUMMARY AND OUTLOOK

Based on the standard SHF, KIDS, and RMF models, we have studied the constraint on the density dependence of the symmetry energy $E_{sym}(\rho)$ from the neutron-skin thickness data of PREX and CREX as well as neutron-star data from GW170817, PSR J0030+0451,

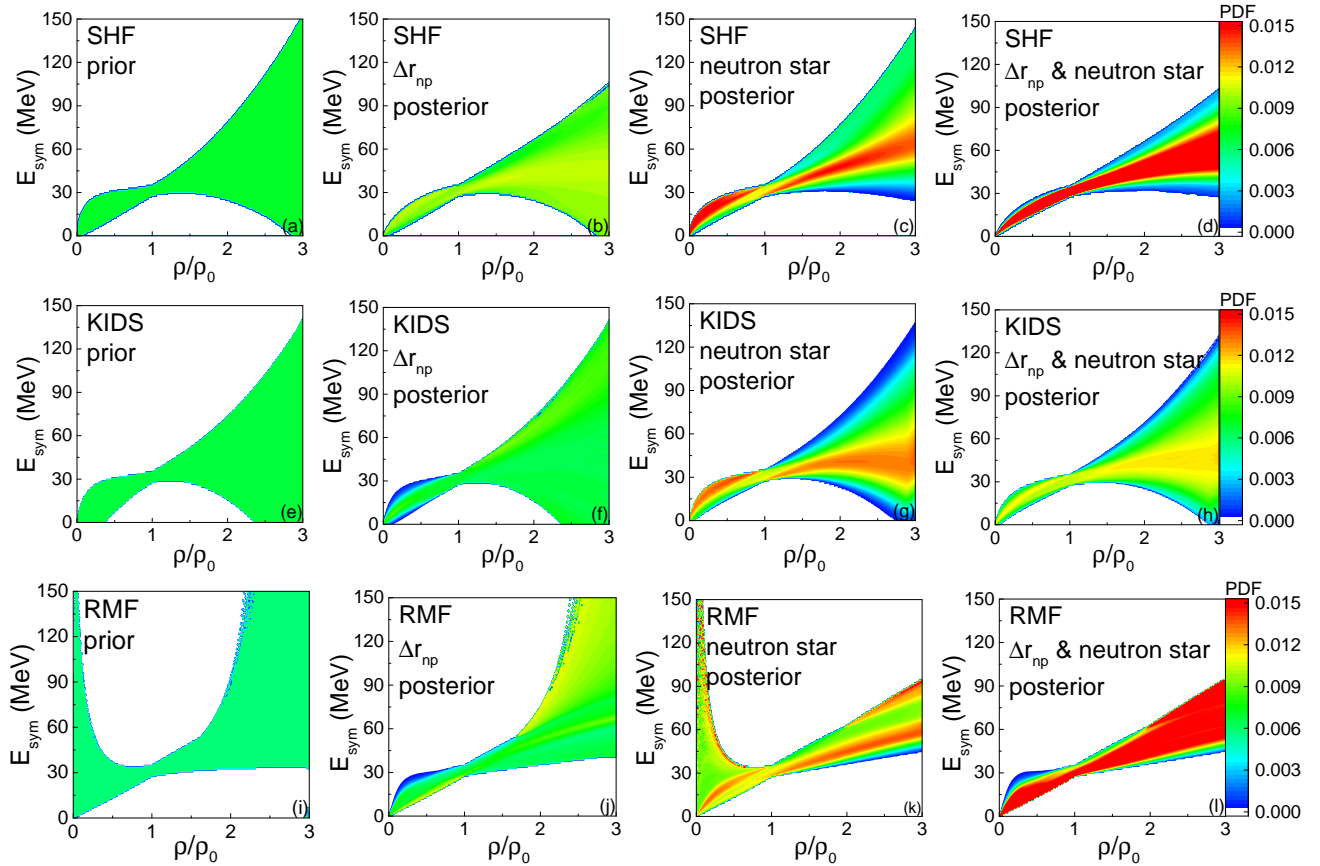


FIG. 4. Prior PDFs and posterior PDFs of the nuclear symmetry energy from the neutron-skin thickness data, neutron-star observables, and both data sets, based on the standard SHF (first row), KIDS (second row), and RMF (third row) models.

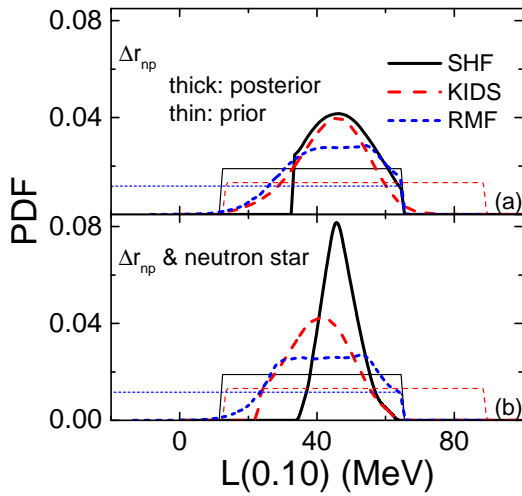


FIG. 5. Posterior PDFs of the slope parameter at $\rho = 0.10 \text{ fm}^{-3}$ from the neutron-skin thickness data (a) and together with neutron-star observables (b), based on the standard SHF, KIDS, and RMF models.

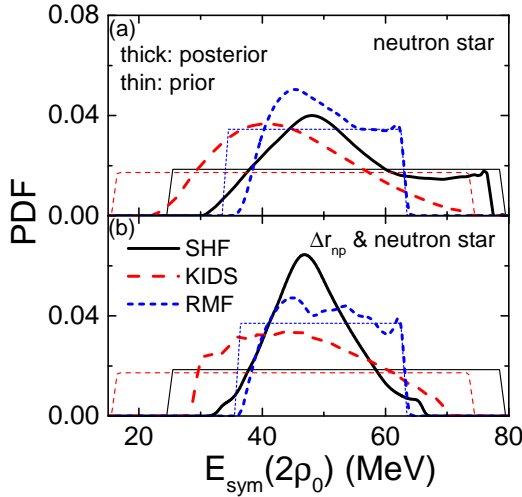


FIG. 6. Posterior PDFs of the nuclear symmetry energy at $\rho = 2\rho_0$ from neutron-star observables (a) and together with the neutron-skin thickness data (b), based on the standard SHF, KIDS, and RMF models.

and PSR J0740+6620 using a Bayesian approach. Despite the soft and stiff symmetry energy favored respectively by the CREX and the PREX data, the Bayesian analysis is able to find a compromise for the $E_{sym}(\rho)$. While the neutron-skin thickness data (neutron-star observables) mostly constrain the $E_{sym}(\rho)$ at subsaturation (suprasaturation) densities, they more or less affect the constraint on the $E_{sym}(\rho)$ at suprasaturation (subsaturation) densities. For the RMF model, we found that the dependence of the neutron-skin thickness on the symmetry energy parameters can be quite different for a small Dirac effective mass ($m_s^*/m < 0.6$) compared to that for a large one ($m_s^*/m > 0.6$), as shown in Fig. 7. While the

key constraints on the $E_{sym}(\rho)$ from the present study can be found in Fig. 4, the slope parameters at $\rho = 0.10 \text{ fm}^{-3}$ are constrained to be 47^{+4}_{-5} MeV for the standard SHF model, 41^{+9}_{-8} MeV for the KIDS model, and $43^{+13}_{-12} \text{ MeV}$ for the RMF model, and the values of $E_{sym}(2\rho_0)$ are constrained to be 49^{+5}_{-7} MeV for the standard SHF model, $46^{+13}_{-9} \text{ MeV}$ for the KIDS model, and 51^{+8}_{-7} MeV for the RMF model, within 68% confidence intervals surrounding its mean value from both neutron-skin thickness data and neutron-star observables.

The constraints on the symmetry energy shown in the right column of Fig. 4 from the neutron-skin thickness data and the neutron-star observables are similar for the three adopted models. On the other hand, some model dependencies do exist, mainly due to the inclusion of higher-order EOS parameters and the difference between relativistic and non-relativistic models. While a model with a smaller number of free parameters is always favored, a more flexible model with more free parameters is capable of extracting the detailed information of the nuclear interaction, as long as more constraints are incorporated from various observables based on the Bayesian analysis.

While the data from parity-violating electron-nucleus scattering experiments are less model-dependent, the large 1σ error bars for the PREX and CREX data reduce the constraining power on the slope parameter L of the symmetry energy and the behavior of $E_{sym}(\rho)$. In future studies, we may adopt more nuclear structure data, including isotope binding energy difference and nucleus resonances, and then hopefully put a more stringent constraint on $E_{sym}(\rho)$.

Appendix A: Sensitivity investigation of neutron-skin thickness for the RMF model

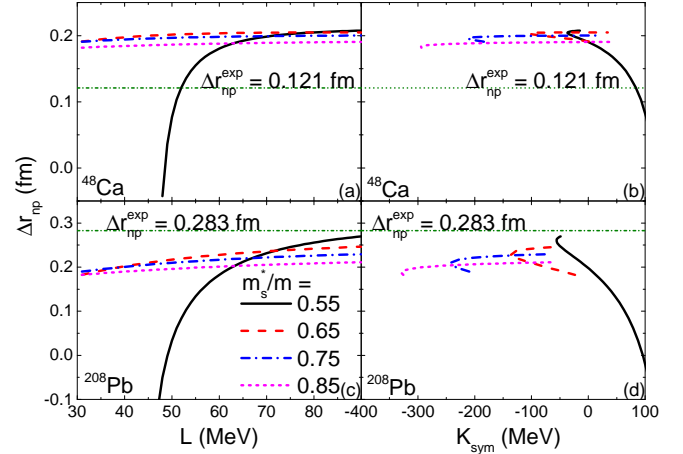


FIG. 7. Dependence of the neutron-skin thickness in ^{48}Ca and ^{208}Pb on the slope parameter L and the curvature parameter K_{sym} of the symmetry energy for different values of isoscalar Dirac mass m_s^* in the RMF model.

To understand the abnormal posterior PDFs of the slope parameter L and the curvature parameter K_{sym} of the symmetry energy from the neutron-skin thickness Δr_{np} data for the RMF model in Fig. 3, we show in Fig. 7 the dependence of resulting Δr_{np} in ^{48}Ca and ^{208}Pb on the corresponding symmetry energy parameters, for different values of isoscalar Dirac mass m_s^* . The illustration is based on an optimized parameter set (K_0 , Q_0 , E_{sym}^0 , L , m_s^*) that reproduces best the data of ^{48}Ca and ^{208}Pb , and then values of L and m_s^* are varied. Since K_{sym} is not chosen as an independent parameter in the RMF analysis, its value changes with L for a fixed m_s^* . For $m_s^*/m = 0.65$, 0.75, and 0.85, Δr_{np} in both ^{48}Ca and ^{208}Pb increases almost linearly with increasing L , while their dependencies on K_{sym} show non-monotonic behaviors. However, they are unable to reproduce the small Δr_{np}^{exp} in ^{48}Ca and the large Δr_{np}^{exp} in ^{208}Pb within the prior range of L . For $m_s^*/m = 0.55$, some abnormal behaviors are observed, and this is due to the too large g_ρ^2/m_ρ^2 value inversely obtained in the RMF model. It is seen that the Δr_{np} in both ^{48}Ca and ^{208}Pb decreases dramatically with decreasing L around $L = 50 - 60$ MeV, or with increasing K_{sym} at $K_{sym} > 0$, for a small m_s^*/m .

At even smaller values of L , we are unable to get inversely the coefficients in the RMF model. For ^{48}Ca , it is seen that the small Δr_{np} can only be well reproduced by a small m_s^*/m and $L = 50 - 60$ MeV, with the latter corresponding to the peak in the posterior PDF of L in Fig. 2(h). The range of $K_{sym} > 0$ is also favored by the small Δr_{np}^{exp} in ^{48}Ca , corresponding to the posterior PDF of K_{sym} in Fig. 2(i). For ^{208}Pb , even for a small m_s^*/m , the large Δr_{np}^{exp} favors a large L , so the posterior PDF of L in Fig. 2(h) looks normal. As can be seen from Fig. 7(d), the large Δr_{np}^{exp} in ^{208}Pb favors a K_{sym} around -50 MeV but disfavors a positive K_{sym} , consistent with the behavior in Fig. 2(i).

ACKNOWLEDGMENTS

We acknowledge helpful discussions with Panagiota Papakonstantinou. This work is supported by the Strategic Priority Research Program of the Chinese Academy of Sciences under Grant No. XDB34030000, the National Natural Science Foundation of China under Grant Nos. 12375125, 11922514, and 11475243, and the Fundamental Research Funds for the Central Universities.

[1] Andrew W. Steiner, Madappa Prakash, James M. Lattimer, and Paul J. Ellis, “Isospin asymmetry in nuclei and neutron stars,” *Phys. Rept.* **411**, 325–375 (2005), [arXiv:nucl-th/0410066](https://arxiv.org/abs/nucl-th/0410066).

[2] James M. Lattimer and Maddapa Prakash, “Neutron Star Observations: Prognosis for Equation of State Constraints,” *Phys. Rept.* **442**, 109–165 (2007), [arXiv:astro-ph/0612440](https://arxiv.org/abs/astro-ph/0612440).

[3] Bao-An Li, Lie-Wen Chen, and Che Ming Ko, “Recent Progress and New Challenges in Isospin Physics with Heavy-Ion Reactions,” *Phys. Rept.* **464**, 113–281 (2008), [arXiv:0804.3580](https://arxiv.org/abs/0804.3580) [nucl-th].

[4] W. G. Lynch and M. B. Tsang, “Decoding the density dependence of the nuclear symmetry energy,” *Phys. Lett. B* **830**, 137098 (2022), [arXiv:2106.10119](https://arxiv.org/abs/2106.10119) [nucl-th].

[5] Zhen Zhang and Lie-Wen Chen, “Constraining the symmetry energy at subsaturation densities using isotope binding energy difference and neutron skin thickness,” *Phys. Lett. B* **726**, 234–238 (2013), [arXiv:1302.5327](https://arxiv.org/abs/1302.5327) [nucl-th].

[6] Jun Xu, Wen-Jie Xie, and Bao-An Li, “Bayesian inference of nuclear symmetry energy from measured and imagined neutron skin thickness in $^{116,118,120,122,124,130,132}\text{Sn}$, ^{208}Pb , and ^{48}Ca ,” *Phys. Rev. C* **102**, 044316 (2020), [arXiv:2007.07669](https://arxiv.org/abs/2007.07669) [nucl-th].

[7] Andrea Maselli, Andrea Sabatucci, and Omar Benhar, “Constraining three-nucleon forces with multimessenger data,” *Phys. Rev. C* **103**, 065804 (2021).

[8] Andrea Sabatucci, Omar Benhar, Andrea Maselli, and Costantino Pacilio, “Sensitivity of neutron star observations to three-nucleon forces,” *Phys. Rev. D* **106**, 083010 (2022).

[9] Yingxun Zhang, Min Liu, Cheng-Jun Xia, Zhuxia Li, and S. K. Biswal, “Constraints on the symmetry energy and its associated parameters from nuclei to neutron stars,” *Phys. Rev. C* **101**, 034303 (2020).

[10] Hana Gil, Young-Min Kim, Panagiota Papakonstantinou, and Chang Ho Hyun, “Constraining the density dependence of the symmetry energy with nuclear data and astronomical observations in the korea-ibs-daegu-skku framework,” *Phys. Rev. C* **103**, 034330 (2021).

[11] Zhenyu Zhu, Ang Li, Jinniu Hu, and Hong Shen, “Equation of state of nuclear matter and neutron stars: Quark mean-field model versus relativistic mean-field model,” *Phys. Rev. C* **108**, 025809 (2023).

[12] Virender Thakur, Raj Kumar, Pankaj Kumar, Mukul Kumar, C. Mondal, Kaixuan Huang, Jinniu Hu, B. K. Agrawal, and Shashi K. Dhiman, “Relativistic approach for the determination of nuclear and neutron star properties in consideration of prex-ii results,” *Phys. Rev. C* **107**, 015803 (2023).

[13] Marc Salinas and J. Piekarewicz, “Bayesian refinement of covariant energy density functionals,” *Phys. Rev. C* **107**, 045802 (2023).

[14] D. Adhikari *et al.* (PREX), “Accurate Determination of the Neutron Skin Thickness of ^{208}Pb through Parity-Violation in Electron Scattering,” *Phys. Rev. Lett.* **126**, 172502 (2021), [arXiv:2102.10767](https://arxiv.org/abs/2102.10767) [nucl-ex].

[15] D. Adhikari *et al.* (CREX), “Precision Determination of the Neutral Weak Form Factor of Ca48,” *Phys. Rev. Lett.* **129**, 042501 (2022), [arXiv:2205.11593](https://arxiv.org/abs/2205.11593) [nucl-ex].

[16] B. P. Abbott *et al.* (LIGO Scientific, Virgo), “GW170817: Measurements of neutron star radii and equation of state,” *Phys. Rev. Lett.* **121**, 161101 (2018), [arXiv:1805.11581](https://arxiv.org/abs/1805.11581) [gr-qc].

[17] Thomas E. Riley *et al.*, “A NICER View of PSR

J0030+0451: Millisecond Pulsar Parameter Estimation,” *Astrophys. J. Lett.* **887**, L21 (2019), arXiv:1912.05702 [astro-ph.HE].

[18] Thomas E. Riley, Anna L. Watts, Paul S. Ray, Slavko Bogdanov, Sébastien Guillot, Sharon M. Morsink, Anna V. Bilous, Zaven Arzoumanian, Devarshi Choudhury, Julia S. Deneva, Keith C. Gendreau, Alice K. Harding, Wynn C. G. Ho, James M. Lattimer, Michael Loewenstein, Renee M. Ludlam, Craig B. Markwardt, Takashi Okajima, Chanda Prescod-Weinstein, Ronald A. Remillard, Michael T. Wolff, Emmanuel Fonseca, H. Thankful Cromartie, Matthew Kerr, Timothy T. Pennucci, Aditya Parthasarathy, Scott Ransom, Ingrid Stairs, Lucas Guillemot, and Ismael Cognard, “A NICER view of the massive pulsar PSR j0740+6620 informed by radio timing and XMM-newton spectroscopy,” *The Astrophysical Journal Letters* **918**, L27 (2021).

[19] Bao-An Li, Bao-Jun Cai, Wen-Jie Xie, and Nai-Bo Zhang, “Progress in Constraining Nuclear Symmetry Energy Using Neutron Star Observables Since GW170817,” *Universe* **7**, 182 (2021), arXiv:2105.04629 [nucl-th].

[20] J. M. Lattimer, “Neutron Stars and the Nuclear Matter Equation of State,” *Ann. Rev. Nucl. Part. Sci.* **71**, 433–464 (2021).

[21] S. Huth *et al.*, “Constraining Neutron-Star Matter with Microscopic and Macroscopic Collisions,” *Nature* **606**, 276–280 (2022), arXiv:2107.06229 [nucl-th].

[22] Lie-Wen Chen, Che Ming Ko, Bao-An Li, and Jun Xu, “Density slope of the nuclear symmetry energy from the neutron skin thickness of heavy nuclei,” *Phys. Rev. C* **82**, 024321 (2010), arXiv:1004.4672 [nucl-th].

[23] Jun Xu and Panagiota Papakonstantinou, “Bayesian inference of finite-nuclei observables based on the kids model,” *Phys. Rev. C* **105**, 044305 (2022).

[24] Wei-Chia Chen and J. Piekarewicz, “Building relativistic mean field models for finite nuclei and neutron stars,” *Phys. Rev. C* **90**, 044305 (2014).

[25] Ying-Yu Cao, Jian-You Guo, and Bo Zhou, “Predictions of nuclear charge radii based on the convolutional neural network,” *Nuclear Science and Techniques* **34**, 152 (2023).

[26] Tian-Shuai Shang, Jian Li, and Zhong-Ming Niu, “Prediction of nuclear charge density distribution with feedback neural network,” *Nuclear Science and Techniques* **33**, 153 (2022).

[27] Wanbing He, Qingfeng Li, Yugang Ma, Zhongming Niu, Junchen Pei, and Zhang Yingxun, “Machine learning in nuclear physics at low and intermediate energies,” *SCIENCE CHINA Physics, Mechanics & Astronomy* **66**, 282001 (2023).

[28] Zepeng Gao and Qingfeng Li, “Studies on several problems in nuclear physics by using machine learning,” *Nuclear Techniques* **46**, 080009 (2023).

[29] Weifeng Li, Xiaoyan Zhang, and Zhongming Niu, “Studies of nuclear β -decay half-lives with bayesian neural network approach,” *Nuclear Techniques* **46**, 080013 (2023).

[30] Wan-Bing He, Yu-Gang Ma, Long-Gang Pang, Hui-Chao Song, and Kai Zhou, “High-energy nuclear physics meets machine learning,” *Nuclear Science and Techniques* **34**, 88 (2023).

[31] Yu-Gang Ma, Long-Gang Pang, Rui Wang, and Kai Zhou, “Phase transition study meets machine learning,” *Chinese Physics Letters* **40**, 122101 (2023).

[32] D. Vautherin and D. M. Brink, “Hartree-Fock calculations with Skyrme’s interaction. 1. Spherical nuclei,” *Phys. Rev. C* **5**, 626–647 (1972).

[33] P.-G. Reinhard, “The skyrme—hartree—fock model of the nuclear ground state,” in *Computational Nuclear Physics 1: Nuclear Structure*, edited by K. Langanke, Joachim A. Maruhn, and S. E. Koonin (Springer Berlin Heidelberg, Berlin, Heidelberg, 1991) pp. 28–50.

[34] Jia Zhou, Jun Xu, and Panagiota Papakonstantinou, “Bayesian inference of neutron-star observables based on effective nuclear interactions,” *Phys. Rev. C* **107**, 055803 (2023), arXiv:2301.07904 [nucl-th].

[35] W Pöschl, D Vretenar, A Rummel, and P Ring, “Application of finite element methods in relativistic mean-field theory: spherical nucleus,” *Computer Physics Communications* **101**, 75–107 (1997).

[36] Jun Xu, Lie-Wen Chen, Bao-An Li, and Hong-Ru Ma, “Nuclear constraints on properties of neutron star crusts,” *Astrophys. J.* **697**, 1549–1568 (2009), arXiv:0901.2309 [astro-ph.SR].

[37] Jun Xu, Lie-Wen Chen, Bao-An Li, and Hong-Ru Ma, “Locating the inner edge of the neutron star crust using terrestrial nuclear laboratory data,” *Phys. Rev. C* **79**, 035802 (2009).

[38] Bennett Link, Richard I. Epstein, and James M. Lattimer, “Pulsar constraints on neutron star structure and equation of state,” *Phys. Rev. Lett.* **83**, 3362–3365 (1999).

[39] James M. Lattimer and Madappa Prakash, “Nuclear matter and its role in supernovae, neutron stars and compact object binary mergers,” *Physics Reports* **333–334**, 121–146 (2000).

[40] J. M. Lattimer and M. Prakash, “Neutron Star Structure and the Equation of State,” *Astrophys. J.* **550**, 426–442 (2001), arXiv:astro-ph/0002232 [astro-ph].

[41] Gordon Baym, Christopher Pethick, and Peter Sutherland, “The Ground State of Matter at High Densities: Equation of State and Stellar Models,” *Astrophys. J.* **170**, 299 (1971).

[42] Kei Iida and Katsuhiro Sato, “Spin-down of neutron stars and compositional transitions in the cold crustal matter,” *The Astrophysical Journal* **477**, 294–312 (1997).

[43] E. Khan, J. Margueron, and I. Vidaña, “Constraining the nuclear equation of state at subsaturation densities,” *Phys. Rev. Lett.* **109**, 092501 (2012).

[44] Jérôme Margueron, Rudiney Hoffmann Casali, and Francesca Gulminelli, “Equation of state for dense nucleonic matter from metamodeling. i. foundational aspects,” *Phys. Rev. C* **97**, 025805 (2018).

[45] S. Shlomo, V. M. Kolomietz, and G. Colo, “Deducing the nuclear-matter incompressibility coefficient from data on isoscalar compression modes,” *Eur. Phys. J. A* **30**, 23 (2006).

[46] G. Colo, U. Garg, and H. Sagawa, “Symmetry energy from the nuclear collective motion: constraints from dipole, quadrupole, monopole and spin-dipole resonances,” *Eur. Phys. J. A* **50**, 26 (2014), arXiv:1309.1572 [nucl-th].

[47] Umesh Garg and Gianluca Colò, “The compression-mode giant resonances and nuclear incompressibility,” *Prog. Part. Nucl. Phys.* **101**, 55–95 (2018), arXiv:1801.03672 [nucl-ex].

[48] Bao-An Li and Xiao Han, “Constraining the neutron-proton effective mass splitting using empirical constraints on the density dependence of nuclear symmetry energy

around normal density,” *Physics Letters B* **727**, 276–281 (2013).

[49] M. Oertel, M. Hempel, T. Klähn, and S. Typel, “Equations of state for supernovae and compact stars,” *Rev. Mod. Phys.* **89**, 015007 (2017).

[50] Ingo Tews, James M. Lattimer, Akira Ohnishi, and Evgeni E. Kolomeitsev, “Symmetry parameter constraints from a lower bound on neutron-matter energy,” *The Astrophysical Journal* **848**, 105 (2017).

[51] Nai-Bo Zhang, Bao-Jun Cai, Bao-An Li, William G. Newton, and Jun Xu, “How tightly is the nuclear symmetry energy constrained by a unitary Fermi gas?” *Nucl. Sci. Tech.* **28**, 181 (2017), arXiv:1704.02687 [nucl-th].

[52] G. Audi, O. Bersillon, J. Blachot, and A. H. Wapstra, “The Nubase evaluation of nuclear and decay properties,” *Nucl. Phys. A* **729**, 3–128 (2003).

[53] I. Angeli, “A consistent set of nuclear rms charge radii: properties of the radius surface $R(N,Z)$,” *Atom. Data Nucl. Data Tabl.* **87**, 185–206 (2004).

[54] Zhen Zhang and Lie-Wen Chen, “Constraining the symmetry energy at subsaturation densities using isotope binding energy difference and neutron skin thickness,” *Physics Letters B* **726**, 234–238 (2013).

[55] Wen-Jie Xie and Bao-An Li, “Bayesian Inference of the Symmetry Energy of Superdense Neutron-rich Matter from Future Radius Measurements of Massive Neutron Stars,” *Astrophys. J.* **899**, 4 (2020), arXiv:2005.07216 [astro-ph.HE].